Investigating the Influence of Flow Rate on Biofilm Growth in Three Dimensions using Microimaging

Sassan Ostvar

School of Chemical, Biological and Environmental Engineering, Oregon State University, Corvallis, Oregon, USA

Gabriel Iltis

School of Chemical, Biological and Environmental Engineering, Oregon State University, Corvallis, Oregon, USA

Yohan Davit

Institut de Mécanique des Fluides de Toulouse (IMFT), Université de Toulouse, CNRS, INPT, UPS, Toulouse, France

Steffen Schlüter

Department of Soil Physics, Helmholtz-Centre for Environmental Research - UFZ, Halle, Germany

Linnéa Andersson

School of Chemical, Biological and Environmental Engineering, Oregon State University, Corvallis, Oregon, USA

Brian D. Wood

School of Chemical, Biological and Environmental Engineering, Oregon State University, Corvallis, Oregon, USA

Dorthe Wildenschild

School of Chemical, Biological and Environmental Engineering, Oregon State University, Corvallis, Oregon, USA

Abstract

We explore how X-ray computed microtomography can be used to generate highly-resolved 3D biofilm datasets on length scales that span multiple pore bodies. The data is integrated into a study of the effects of flow rate on three-dimensional growth of biofilm in porous media. Three flow rates were investigated in model packed-bed columns. Biofilm growth was monitored during an 11-day growth period using a combination

of differential pressure and effluent dissolved oxygen measurements. At the end of the growth period, all columns were scanned using X-ray computed microtomography and a barium sulfate-based contrast agent. The resulting images were prepared for quantitative analysis using a novel image processing workflow that was tailored to this specific system. The reduction in permeability due to biofilm growth was studied using both transducer-based pressure drop measurements and image-based calculations using the Kozeny-Carman model. In addition, a set of structural measures related to the spatial distribution of biofilms were computed and analyzed for the different flow rates. We generally observed 1 to 2 orders of magnitude decrease in permeability as a result of bioclogging for all columns (i.e, across flow rates). The greatest average permeability and porosity reduction was observed for the intermediate flow rate (4.5 ml/hr). A combination of results from different measurements all suggest that biofilm growth was oxygen limited at the lowest flow rate, and affected by shear stresses at the highest flow rate. We hypothesize that the interplay between these two factors drives the spatial distribution and quantity of biofilm growth in the class of porous media studied here. Our approach opens the way to more systematic studies of the structure-function relationships involved in biofilm growth in porous media and the impact that such growth may have on physical properties such as hydraulic conductivity.

---

1. Introduction

The interaction of hydrodynamics and biofilm growth in media with tortuous geometries is of great scientific interest because of its prevalence in many natural and engineered systems (Drescher et al., 2013). As examples, biofilm growth in porous media has been both directly observed and indirectly hypothesized (with substantial supporting evidence) in a wide variety of natural and engineered systems. These include examples such as anaerobic reactors (e.g. Young and Dahab (1983)), microbially-enhanced oil recovery (e.g. Armstrong and Wildenschild (2012); Sen (2008)), micromodel experiments (e.g. Kim and Fogler (2000); Stewart and Fogler (2001)), laboratory porous media experiments (e.g. Vogt et al. (2013)), and slow sand filter beds (e.g. Li et al. (2013)). Although there are ongoing discussions regarding the ubiquity of biofilms (Baveye and Darnault, 2017; Coyte et al., 2017), these studies offer significant, and often direct, evidence that biofilm formation in porous media is an important component for many processes of relevance and interest.

In natural and synthetic porous media, biofilm growth at the pore scale affects various transport processes by altering the structure of interfaces, connectivity of the pore space, and bulk geometric properties of the medium (Baveye et al., 1998; Cunningham et al., 1991; Drescher et al., 2013; Rittmann, 1993). In turn, cellular growth and mesoscale structural evolution of biofilms are highly interconnected with various aspects of transport including shear and mass transfer. Non-destructive imaging of biofilms is essential to understanding the physics of these processes and their broader impacts on design, control, and prediction.

In disciplines that are concerned with natural porous media (e.g. hydrology, petroleum engineering), the ability to visualize biofilm growth under flow on the scale of millimeters to meters has been of great interest (e.g. Thullner (2010); Yarwood et al. (2002)). Visualization is gaining even more significance with the increasing complexity and fidelity of the mathematical and computational approaches to modeling biofilm growth in porous media (e.g. von der Schulenburg et al. (2009)). The challenges associated with

non-intrusive visualization of 3D systems often forces direct comparison between models and experiments to rely on bulk (aggregate) laboratory or field measurements; i.e. evaluations on scales where pore-scale (structural) information detrimental to transport is lost to the averaging inherent to measurements (Thullner, 2010).

Magnetic Resonance Microscopy (MRM) and Nuclear Magnetic Resonance imaging (NMR) have been successfully applied to elucidate the global structure of biofilms in porous media and pore fluid velocities in media altered by microbial growth (Manz et al., 2003; Seymour et al., 2004, 2007), albeit with some resolution limitations. Confocal laser scanning microscopy (CLSM), and more recently optical coherence tomography (OCT), have been successfully applied to the visualization of the 3D structure of biofilms on smaller scales with higher resolutions (Davit et al., 2013; Dreszer et al., 2014; Neu and Lawrence, 2015; Wagner et al., 2010; Xi et al., 2006). Both methods enable temporal studies of growth in flow environments, and provide highly resolved reproductions of the internal structure of the biofilm matrix. A popular approach to direct visualization of biofilm structure in porous media at the pore scale has been to adopt these techniques to study growth in optically transparent (Leis et al., 2005), 2D and pseudo-3D micromodels (e.g. Beyenal et al. (2004); Kim and Fogler (2000); Rodríguez and Bishop (2007); Stoodley et al. (1999)).

A limitation in extending this methodology to study biomass formation in 3D porous media is that experimental systems must be optically transparent, small enough to fit onto the microscope stage, and in the case of CLSM, thin enough to fit within the focal range of the device. Conversely, 3D porous systems are opaque and deep. Whether or not the conclusions drawn for 2D systems can be extended to 3D is an unanswered question. Topologically, the two are not equivalent (e.g., diffusions in 2- and 3-dimensions are fundamentally different), so one would not expect 2-dimensional experiments to capture the range of physical behaviors. Thus, the literature's prevailing answer to this question seems to be negative (e.g. see the discussion by Thullner (2010) and Baveye (2010)).

X-ray computed microtomography (CMT) is emerging as an alternative that enables

4

visualization of biofilms in 3D in opaque media (Davit et al., 2011; Iltis et al., 2011; Wildenschild and Sheppard, 2013) on the pore scale. Though still in its infancy, the method was originally developed and explored using both polychromatic (Davit et al., 2011) and monochromatic synchrotron-based systems (Iltis, 2013; Iltis et al., 2011). Users can expect voxel resolutions on the order of 1-2 microns to be easily achieved. The technique relies on the use of contrast agents to facilitate the adsorption-based detection of different phases within an opaque sample using X-rays. Central to the method is creating a physical mechanism that allows image processing to differentiate between the fluid and biofilm phases, the natural attenuation (photon cross-section) of which are almost identical.

Use of different contrast agents, added to the aqueous phase, such as silver-coated hollow microspheres (Iltis et al., 2011), barium sulfate suspensions (Davit et al., 2011; Iltis, 2013), and 1-chloronaphtalene (du Roscoat et al., 2014; Ivankovic et al., 2017) have shown promise. Similarly, adding $FeSO_4$ as a contrast agent to the biofilm phase, and using the free space propagation of X-rays to bring out additional refractive effects, Carrel et al. (2017) were also able to image biofilms in opaque porous media. The latter study compared the $FeSO_4$ to the $BaSO_4$ method and found differences in the amount of biofilm imaged, with a significantly larger amount of biofilm identified using the $FeSO_4$ method. The authors pointed out three possible reasons for the discrepancy; (i) partial volume effects (eliminated from consideration); (ii) uncertainty related to the segmentation (caused by the significant heterogeneity of the biofilm phase and poor contrast of said phase); and (iii) interaction between the $BaSO_4$ and the biofilm (causing suspended biomass and loosely attached components of the biofilm to be washed out of the columns).

The potential for detachment of biofilm during addition of a denser and more viscous (aqueous phase) contrast agent has been discussed by Davit et al. (2011) and du Roscoat et al. (2014). In a thorough study of the problem, Ivankovic et al. (2017) found that this effect can be eliminated by using smaller beads (in their case, less than 2mm) and by making measurements after longer periods of biofilm growth (> 7 days) such

that a more compact and tightly attached biofilm was formed. This allowed for reliable studies on biofilms that presented similar and reproducible spatial structure and allowed for quantitative evaluation of a number of different environmental variables. In their study, growth periods of less than 3 days, and larger pore sizes, resulted in less resilient biofilms (exhibiting streamers and other weakly attached components) that may be subject to detachment shear by a more viscous contrast agent (such as $BaSO_4$ or 1-chloronaphtalene). For the 1-chloronaphtalene (CN) an additional challenge was caused by the oily nature of the contrast agent, which caused pendular rings of CN to be left behind at bead contacts.

The exact growth period and pore size that will produce repeatable experiments will vary somewhat with organism, nutrient supply, flow rate (all factors contributing to the production of more or less dense biofilms), and the viscosity of the injected contrast agent (if relevant). The past studies using *aqueous* phase contrast agents serve as promising proof of the concept as long as the risk of viscous interaction with the biofilm is considered in the design of the experiments. While there is less risk of detachment using a contrast agent in the *biofilm* itself (Carrel et al., 2017), the resulting weak contrast between the various phases makes reliable and objective quantitative evaluation difficult.

In this study, we present a systematic study on the correspondence between physical quantities derived from CT data and physical measurements of biofilm growth; such a comparison has yet to be reported in the literature. Our data consists of duplicate columns grown for 11 days to ensure a dense and resilient biofilm. The resulting image histograms exhibit distinct separation of the intensity peaks (indicative of effective phase separation) and we use advanced image processing methods to allow for objective measurements of a number of biofilm features as a function of Reynolds number (Re).

When possible, we cross-validate the results obtained via microimage analysis with those obtained via direct bulk measurements. Numerous studies conducted on bioclogging in porous media under various conditions have reported significant reductions in hydraulic conductivity, often up to 2-3 orders of magnitude or more (Bielefeldt et al.,

2002; Cunningham et al., 1991; Seifert and Engesgaard, 2007; Thullner, 2010; Vandevivere and Baveye, 1992). Due mainly to limitations in measuring or imaging the spatial distribution of biomass, however, only a few reports have attempted to associate changes in pore morphology with changes in hydraulic conductivity in 3D, mostly indirectly or via destructive sampling. A number of authors have observed that a majority of the biomass and associated clogging occurred within the first several centimeters of the experimental apparatus (e.g. Seifert and Engesgaard (2007)). Others have argued that bioclogging should be attributed primarily to blockage of pore throats by biomass as opposed to uniform continuous films on solid surfaces (e.g. Vandevivere et al. (1995))

2. Methods

By building on the work of Davit et al. (2011), we study flow rates that span three orders of magnitude (corresponding to initial pore-scale Re of 0.1, 1.0, and 10), covering creeping to mildly laminar flows. We are particularly interested in characterizing the global biofilm structure grown under the stipulated flow conditions and tracing these variations to bulk measurements. The work introduces a simple analysis of biofilm growth within opaque porous media based on 3D structural measures along with correlation to (i) bulk pressure drop measurements and (ii) dissolved oxygen consumption to evaluate potential nutrient limitations imparted by the applied flow rates. Our analysis relies on a novel image processing workflow that addresses some of the limitations associated with inhomogeneous distribution of the contrast agent in the pore space.

2.1. Model Porous Medium

Packed bead column reactors measuring 6.3 mm in diameter, 42 mm in length, with a 25-mm clear window were constructed of polycarbonate tubing. The porous medium consisted of soda-lime silica glass beads, with particle diameter within the range 1.4 to 1.7 mm, and specific gravity of 2.5. A total of 6 growth reactors were used in this study, so that there were duplicate columns examined at each flow rate. Initial column porosities were measured gravimetrically prior to the experiments and

7

initial flow testing was conducted to measure the hydraulic conductivity of the models as described below.

2.2. Microbial Species

The bacterium used in this study is *Shewanella oneidensis* MR-1; a metal-reducing strain originally isolated from sediment from Lake Oneida in New York. *S. oneidensis* MR-1 is a gram-negative, highly piliated, polarly flagellated, facultative anaerobe capable of dissimilatory metal reduction and biofilm formation (Majors et al., 2005; Venkateswaran et al., 1999). The bacterium is motile; the presence of pili are critical to initial adhesion and the flagella have been identified as being critical for development of effective biofilm structure (Thormann et al., 2004). The bacterium has also been shown to be motile in response to low oxygen tensions (Thormann et al., 2005). This strain has been used successfully in previous biofilm imaging studies conducted by our group (Iltis et al., 2011).

2.3. Growth Media and Conditions

Inocula were grown from frozen stock for two growth cycles. Initially, frozen stock was thawed and 0.5 mL stock culture was added to 30 mL sterile 100% (30 g/L) Tryptic Soy Broth (TSB). Batch cultures were grown on an incubated shaker table at 250 rpm and 30°C for 20 hours at which point the second growth cycle was started by adding 1 mL of batch culture from the first growth cycle to 30 mL fresh, sterile 100% TSB growth media. Batch cultures were then incubated for another 20-hour cycle. At the conclusion of the second growth cycle, batch cultures were centrifuged at 6000 rpm for 10 minutes, the supernatant was poured off, and the cell pellets were resuspended in 5 mL 100% TSB (30 g/L) growth media for column inoculation.

All column growth reactors and tubing were sterilized prior to inoculation by flushing a 90% ethanol solution through the test apparatus for 30 min, at which point a growth media flush commenced to ensure that all ethanol was removed from the system prior to inoculation. The sterile 10% TSB-saturated columns were then injected with 1 mL of the concentrated cell inoculum. A 24 hour no flow period was allowed to promote

8

biofilm nucleation, after which flow of sterile oxygenated growth media was started at the prescribed flow rates.

Inocula for the initial growth period were prepared in 100% (30 g/L) tryptic soy broth (TSB) solutions. The medium was diluted down to 10% (3 g/L) for the flow experiments. All growth media were sterilized prior to injection, and continuously aerated using 0.22 μm filtered ambient air. A consistently oxygen-saturated injection with an average influent O_2 concentration of 8.05 ± 0.29 (mg/L) was maintained in the flow experiments.

Three flow rates in the creeping and mildly laminar regimes were targeted for investigation. The corresponding initial Re were 0.1, 1 and 10, where the Re is evaluated for a packed bed using (Gunjal et al., 2005)

$$Re = \frac{1}{(1-\varphi)} \frac{\rho \, v_s D}{\mu} \tag{1}$$

Here, ρ (g/mL) is the density of the fluid phase, D (cm) is a characteristic pore length for the porous medium, taken to be the average grain size; μ (g/cm/hr) is the dynamic viscosity of the fluid phase; and φ is the bulk porosity; and v_s (cm/hr) is the superficial (Darcy) velocity defined as

$$v_s = \frac{Q}{A} \tag{2}$$

where Q (mL/hr) is the fluid flow rate A (cm^2) is the cross-sectional area without the porous medium. Note that φ changes during the course of the experiments so the above values represent Reynolds numbers at the onset of growth. For the model systems used in this study, these values correspond to flow rates of 4.5, 45, and 450 (mL/hr). These values are referred to as the *lowest*, *intermediate*, and *highest* flow rates throughout the text.

Continuous flow was provided to each column growth reactor using continuous-cycle syringe pumps. Check valves were used to ensure that flow through the reactor columns was always unidirectional. A schematic of the experimental setup is provided
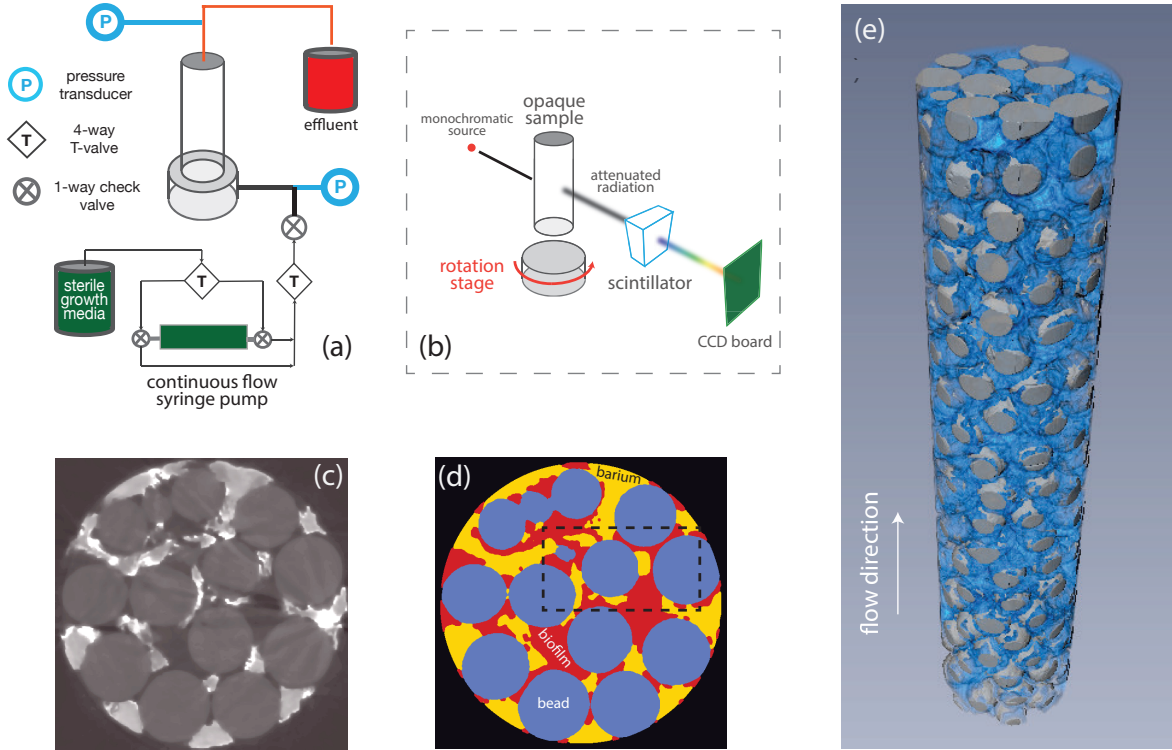
Figure 1: Schematic for experimental flow apparatus (a). Schematic for synchrotron-based X-ray microtomographic imaging of the 3D opaque samples (b). Sample cross-sectional grey-scale image of a column after biofilm growth (dark circular grey areas are glass beads) (c). The same sample after segmentation using the modified Markov Random Field algorithm (blue = glass beads, red = biofilm, and yellow = fluid) (d). 3D reconstruction of a segmented porous medium after biofilm growth at $Re = 10$ (e) (dark gray = beads, blue = biofilm). The dashed rectangular area in (d) is analyzed in detail in Figure 2.

in Figure 1a. Growth media reservoirs were replaced at approximately 36-hr intervals, and all influent lines were replaced every two days to minimize biofilm growth upstream of the experimental columns. Biofilm growth was allowed to continue under constant flow conditions for 11 days, at which point the columns were disconnected and prepared for imaging.

2.4. Differential Pressure Measurement

Differential pressure transducers (Honeywell Sensing and Control, 24PC Series, Columbus OH, USA) were affixed to each experimental column at the column entrance and exit in order to allow for measurement of differential pressure across each column length. Continuous differential pressure measurements were collected by an automated

10

data acquisition system (Personal DAQ 50, Measurement Computing Corp., Norton, MA).

2.5. Dissolved Oxygen Measurement

Periodic measurements of dissolved oxygen (DO) were performed on the influent and effluent sides of each column for the duration of the biofilm growth phase of the experiment. Effluent DO was measured using flow-through oxygen microprobes (Model 16-730, Microelectrodes Inc., Beadford NH, USA). Influent DO measurements were made using a separate probe (Symphony, VWR International) on samples extracted from the sterile media reservoirs. The equipment for measuring influent and effluent dissolved oxygen were kept separate for the duration of the experiment in order to prevent contamination. Dissolved oxygen probes were cleaned using a Tergazyme (Alconox.Inc, White Plains NY, USA) protein removal solution after every set of measurements.

2.6. Computed X-ray Microtomography Imaging

X-ray CMT imaging was conducted at the Advanced Photon Source (APS) facility at Argonne National Laboratory using beamline 13BMD at GSECARS (GeoSoilEnviro Consortium for Advanced Radiation Sources). Immediately prior to imaging, sample columns were disconnected from influent and effluent lines, and injected with the contrast agent solution. The contrast agent consisted of a medical grade barium sulfate ($BaSO_4$) suspension (Micropaque, Guerbet) mixed with sterile growth media. The 1.0 g/mL stock suspension was diluted down to a usable concentration of 0.33 g/mL. The contrast agent was injected into the sample columns using a syringe pump at a rate of 1.2 mL/hr for the $Re = 0.1$ and 1.0 columns, and 5 mL/hr for the $Re = 10$ columns. A total of 2 mL of contrast agent solution was injected into each column.

The average pore volume prior to column inoculation is approximately 0.5 mL, so approximately 4 pore volumes of contrast agent was added to each column. The diluted solution (0.33 g/mL) was selected to balance the absorption of X-ray through the columns with the saturation limit of the X-ray detector (CCD camera). Interested readers are referred to Iltis (2013) for a thorough discussion of barium sulfate concen-

tration ranges for synchrotron-based X-ray CMT of biofilms, where it was reported that the useful range of barium concentration for columns 5 to 7 mm in diameter is 33% (0.33 g/mL) to 50% (0.5 g/mL) barium sulfate.

The K-shell absorption edge for barium is 37.4 keV so each column section was scanned at two energies, one above (37.54 keV) and one below (37.34 keV) this edge. The entire length of each column was scanned by moving the sample stage vertically and generating a series of overlapping scan sections. Volumetric reconstruction of each section was obtained from a series of two-dimensional scans that are obtained via a 180° rotation of the sample stage over 720 increments at each height. The choice of 720 angles is based on experience with the instrumentation at this particular beam-line. The theoretical number of projection angles required is the number of pixels the area of interest covers (as the sample rotates 360 degrees) multiplied by 1.5 (or 540 angles). By oversampling with 720 angles, blur is reduced and the resulting images are of a higher quality; this allows more accurate segmentation and subsequent quantitative analyses.

2.7. Image Processing and Quantitative Analysis

The reconstructed datasets have dimensions of 695 $\times$ 695 $\times$ 470 voxels, a voxel resolution of 10.5 μm and are stored with 16-bit precision. As a first preprocessing step a cylindrical region of interest (ROI) inside the core was extracted. A total variation filter was applied for denoising and an unsharp mask filter used for edge enhancement (Schlüter et al., 2014). Image segmentation of the grayscale data focused on isolating three phases: the biofilm, the $BaSO_4$ suspension (representing the aqueous phase) and the solid phase (glass beads). For these data, proper segmentation required the development of a novel segmentation algorithm that incorporated complementary information from various image sources. Direct isolation of the $BaSO_4$ was facilitated using the increased absorption in the above-Ba-edge vs. below-Ba-edge data sets, which is reflected by high intensity in a difference image. However, the $BaSO_4$ suspension had small-scale heterogeneity due to locally varying barium concentrations, likely a side effect of using a barium concentration on the low end of the applicable concentration range of 33% to 50%. The beads and the biofilm exhibited homogeneous and independently

12

distinguishable X-ray absorption at both the above and below edge scanning energies (Figure 1 in the Appendix). Isolation of the beads and biofilm was accomplished using the below-edge image data sets.

A Markov random field (MRF) segmentation algorithm (Kulkarni et al., 2012; Schlüter et al., 2014) was extended to allow for multiple class statistics from various image sources. At the core of this method, the following minimization problem is solved

$$\hat{C} = \underset{\hat{C}}{argmin} \left[\underbrace{\int_{\mathbf{x} \in \Omega} \int_{\mathbf{x} \in \Lambda} \alpha_\lambda \left(\sqrt{2\pi\sigma_{c,\lambda}^2} + \frac{I'_\lambda(\mathbf{x}) - \mu_{c,\lambda}}{2\sigma_{c,\lambda}^2} \right) d\Lambda(\mathbf{x}) d\Omega(\mathbf{x})}_{\text{class statistics}} + \underbrace{\int_{\mathbf{x},\mathbf{y} \in \Pi} \gamma(c(\mathbf{x}), c(\mathbf{y})) \, d\Pi(\mathbf{x}, \mathbf{y})}_{\text{class boundaries}} \right] \tag{3}$$

with

$$\gamma(c(\mathbf{x}), c(\mathbf{y})) = \begin{cases} -1, & c(\mathbf{x}) = c(\mathbf{y}) \\ +1, & c(\mathbf{x}) \neq c(\mathbf{y}) \end{cases} \tag{4}$$

Here, Ω is the population of all voxels, Π is the population of all pairs of neighboring voxels x and y, Λ is the set of image sources, $c(x)$ is the class label at x, $\mu_{c,\lambda}$ and σ^2 are class mean and variance in a specific image λ, $I'_\lambda(\mathbf{x})$ is the gray value of voxel x in image λ and α_λ is a user-defined image-specific weighting factor that determines the contribution of each likelihood term for a given class relative to the penalty term for class boundaries. In other words, a class label at a certain location is very likely, if (i) the local gray values in all images is close to the specific class mean for these images and if (ii) the majority of neighbors already belong to the same class. Class updating was achieved in a deterministic order denoted as iterative conditional modes (ICM), i.e. starting at one corner of the image the label for each voxel was replaced by the class that minimizes the contribution to Eq 4. The algorithm was stopped after three loops. Values for $\mu_{c,\lambda}$ and σ^2 have to be determined prior to segmentation, which was

13

done by evaluating the joint probabilities, as explained in the Appendix. Classification errors in the MRF segmentation results, due to partial volume effects, were removed via post-processing, which is also explained in the Appendix. The entire workflow from preprocessing to image segmentation and post-processing is based on the QuantIm image processing library (Schlüter et al., 2014; Vogel et al., 2010).

The vertical series of eight segmented volumes is subsequently merged into one column via landmark registration in Avizo Fire 8.3. That is, two consecutive volumes overlapping by 25% and pairs of identical coordinates within these overlap regions have to be identified by tracking easily identifiable features. Figure 1e depicts the merged column for a sample grown under high flow rate conditions (450 mL/hr, $Re = 10$) after segmentation.

The columns are analyzed for each vertical section individually in order to detect changes with respect to inlet distance. The investigated properties comprise standard properties like porosity, biofilm volume, biofilm surface area, biofilm thickness and volume percentage attached to sidewalls. In addition, the spatial patterns of growth and attachment are characterized with three normalized indexes that cover different aspects of biofilm configurations, as demonstrated for a small subset in Figure 2.

The connectivity index (CI) characterizes whether the biofilm is well or poorly connected by means of the Euler characteristic χ. This topological measure is defined as (Vogel et al., 2010)

$$\chi = \mathcal{N} - \mathcal{L} + \mathcal{O} \tag{5}$$

where $\mathcal{N}$ is the number of isolated objects of the material of interest, $\mathcal{L}$ is the number of redundant connections within all material clusters and $\mathcal{O}$ is the number of cavities (e.g. isolated background clusters completely enclosed by the material). The Euler characteristic of the entire pore space in a bead pack (χ_{ps}) is usually negative, because it is well connected with a high number of redundant loops around the beads ($\mathcal{L}$). A normalized connectivity index for the biofilm can the be computed as from the Euler

14

characteristic of the biofilm (χ_{bf}) (Herring et al., 2015) as

$$CI = \frac{\chi_{bf}}{\chi_{ps}} \tag{6}$$

Here, $CI < 1$ indicates an impairment in biofilm connectivity due to the presence of flow channels of barium sulfate solution, whereas $CI > 1$ implies that the coexistence of biofilm and $BaSO_4$ solution within the pore space even increases the number of redundant loops within the biofilm network.

The pore size index (PSI) is based on the analysis of pore diameters by the maximum inscribed sphere method (Figure 2b). The PSI is the ratio of the average pore diameter occupied by biofilm (d_{bf}) divided by the average pore diameter of the entire pore space (d_{ps})

$$PSI = \frac{d_{bf}}{d_{ps}} \tag{7}$$

For this metric, $PSI < 1$ indicates preference of biofilm to occupy pore constrictions and avoid larger pore bodies.

The solid distance index (SDI) is based on the analysis of Euclidean distances from any location in the pore space to the closest solid phase voxel (Figure 2c). The SDI is constructed by normalizing the average distance within the region occupied by the biofilm (e_{bf}) by the average distance of the entire pore space (e_{ps})

$$SDI = \frac{e_{bf}}{e_{ps}} \tag{8}$$

For this metric, $SDI < 1$ indicates preference of biofilm to attach to solid surfaces and avoid pore centers. All quantitative analyses were carried out with Avizo Fire 8.3 and QuantIm.
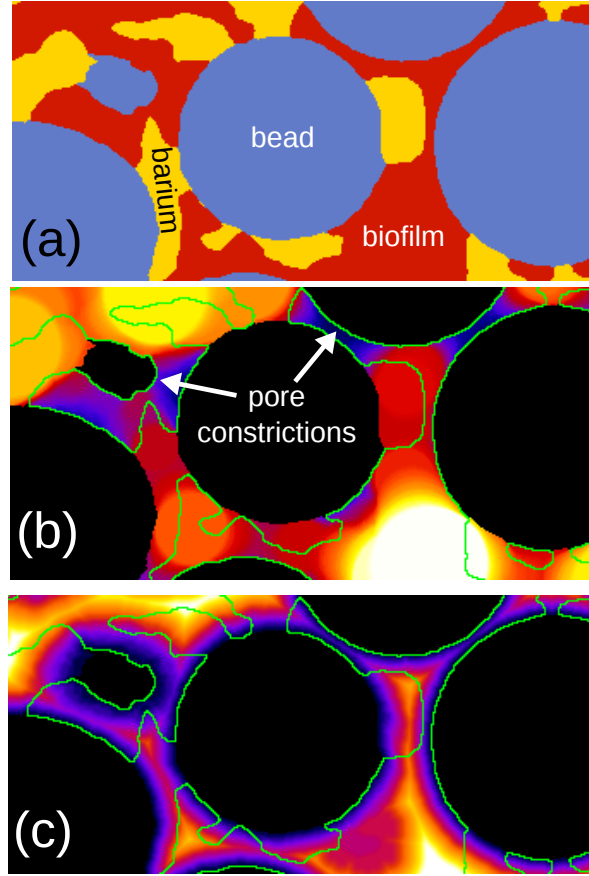
Figure 2: Small subset of segmented CT image occupied by beads, biofilm and BaSO$_4$ solution (a); the connectivity index is based on the topology of the biofilm network. Pore diameters obtained with the maximum inscribed sphere method (b); the pore size index (PSI) is based on the average pore diameter occupied by the biofilm (green). Solid distances in the pore space (c); the solid distance index (SDI) is based on the average solid distance within the biofilm (green).

2.8. Hydraulic Conductivity

Transducer-based hydraulic conductivities were calculated using Darcy's law written for unidirectional axial flow (Bear, 2013)

$$v_z = -\frac{\kappa_{zz}}{\mu} \left(\frac{\partial p}{\partial z} - \rho g \right) \tag{9}$$

where v_z is the superficial velocity (m/s), κ_{zz} the axial component of the permeability tensor (m^2), g the gravitational constant (m/s^2), and $\partial p/\partial z$ the pressure gradient (Pa/m). Equation 9 can be written in the following simplified form for the experimental system

16

$$\frac{Q}{A} = -K \frac{\Delta \Phi}{L} \tag{10}$$

Here $\Delta \Phi$ is the net hydraulic head change across the column (m), L the total length of the column (m), and K the hydraulic conductivity (m/s) that is related to permeability by $K = \kappa_{zz} \rho g / \mu$. Note that the hydraulic head is defined by Hubbert's potential $\Phi(z) = z + p(z)/(\rho g)$, so that $\Delta \Phi$ simply represents the change in the hydraulic head between the inlet and the outlet of the columns, $\Delta \Phi = \Phi_{outlet} - \Phi_{inlet}$.

Transducer-based hydraulic conductivities for sample porous media are usually estimated by scanning a range of flow rates and producing a linear fit to the corresponding pressure drops. Here, in order to reduce uncertainties introduced by transducer noise in the fit, a wide range of flow rates ($0 \ mL/h$ to $2500 \ mL/h$) were applied. This interval extends slightly beyond where Eq 10 is valid into a transitional regime where pressure drop and flow rate are nonlinearly correlated (Bear, 2013). To accommodate for this non-linearity, the Darcy-Forchheimer equation with a quadratic-in-velocity correction was used instead in calculating the pre-growth conductivities.

Post-biofilm-growth hydraulic conductivities and uncertainties were calculated using Eq 10. A potential cause of uncertainty in the measurement was biofilm growing in the inlet tubing, this leading to a decrease of pressure drop, ΔP_{tubing}, when the inlet tubing was changed (Section 2.3). We therefore calculated a lower bound of the permeability using the values of pressure drop averaged over the last 10 hours of each experiment, and an upper bound by subtracting the corresponding ΔP_{tubing} from the average pressure drop.

Image-based hydraulic conductivities were calculated using the following Kozeny-Carman relationship (Bear, 2013) to compare it to transducer-based estimates

$$K = \frac{\rho g}{\mu} \frac{1}{\beta \tau^2} \frac{1}{\mathcal{S}^2} \left[\frac{\varphi^3}{(1 - \varphi)^2} \right] \tag{11}$$

In this expression, the parameters are defined as previously; in addition, $\mathcal{S}$ is the specific surface area (the interfacial surface area to volume ratio of the solid phase), τ is the

tortuosity of the medium, and β is a constant. For simple granular media the prefactor $1/\beta\tau^2$ is usually assumed to be equal to 1/5 (Bear, 2013). We calculated the pre-growth $\mathcal{S}$ directly from the 3D images using values obtained for the glass bead phase in the dry scans. The post-growth $\mathcal{S}$ was calculated by considering the biofilm and glass beads as the solid phase. The sum of the interfacial areas of biofilm and glass beads that were exposed to the pore space was used for this purpose.

One way to calculate K using Eq 11 is to compute the global values for φ and $\mathcal{S}$ as width-weighted averages of all the sections. However, averaging tends to eliminate quite a lot of pore-scale information especially when the biofilm phase is non-uniformly distributed axially. Instead, Eq. 11 was used to compute the hydraulic conductivity of each column section independently and, in analogy with thermal or electrical resistance, the *equivalent* (effective) hydraulic conductivity (K_{eq}) of a column was calculated as the harmonic mean of the constituent sections (Bear, 2013)

$$\frac{L}{K_{eq}} = \sum_{i=1}^{N} \frac{L_i}{K_i} \tag{12}$$

where L is the total length of the evaluated region (cm), L_i is the length of section i (cm), N is the total number of sections, and K_i is the hydraulic conductivity of section i. Treating each imaged section as an independent layer (L_i) allows for a more realistic way of accounting for non-uniform spatial distribution of biofilms and their effect on K.

3. Results

3.1. Porous media characterization

Bulk characterization of the porous media prior to flow experiments provides a simple first check on the self-consistency of imaging and the post-processing workflow. To compare with gravimetric results, global image-based porosity was calculated as a weighted average of the values for different column sections. The bulk and image-based initial column porosities were 0.4000±0.0075 and 0.4000±0.0089, respectively. This
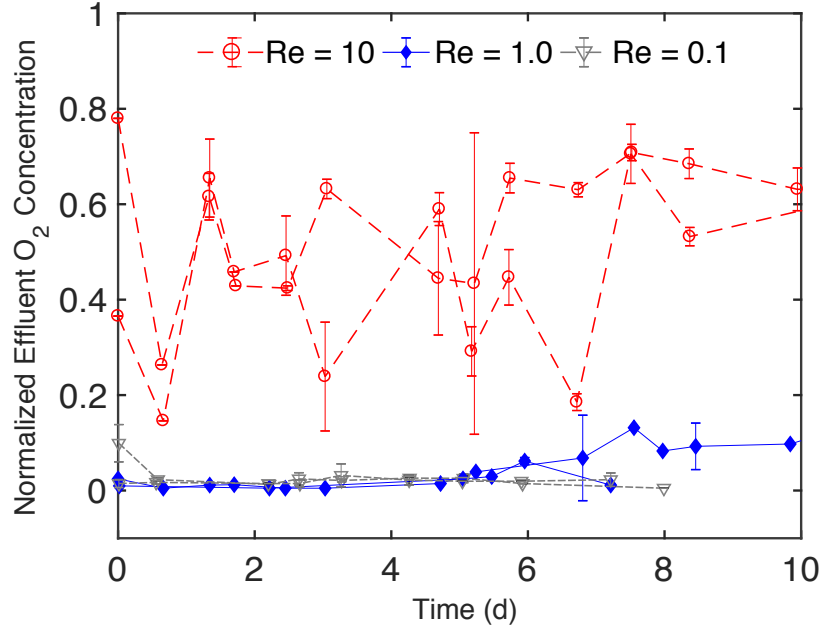
Figure 3: Temporal record of the effluent dissolved oxygen concentration (normalized by the influent concentration) for the 6 experimental columns. Each column in the figure represents measurements made at the corresponding Reynold's number at the onset of the experiment.

excellent match is rather surprising and a strong argument for the adequacy and robustness of the developed image processing workflow. The pre-growth bulk and image-based hydraulic conductivities (K) were 0.0181 ± 0 (cm/s) and 0.0207 ± 0.0019 (cm/s), respectively, demonstrating very good agreement between the two methods. These values are consistent with the general range of values reported for simple granular media (Bear, 2013). The average surface-area-to-volume ratio of the media, $\mathcal{S}$, prior to growth was calculated to be 4.22 ($1/mm$).

3.2. Oxygen utilization

The measured effluent dissolved oxygen concentrations normalized by the influent concentration are reproduced in Figure 3. Influent DO concentrations remained stable around the saturation limit for oxygen in the growth media for the duration of the experiment (the estimated saturation limit was 8.05 ± 0.29 mg/L, which was used to normalize the values in Figure 3). Oxygen utilization showed a marked sensitivity to flow rate. The columns subjected to the lowest flow rate maintained almost negligible

effluent oxygen concentrations. The intermediate flow rate produced a similar curve but showed late-time recovery for at least one of the columns. In sharp contrast, the highest flow rate columns produced a more dynamic response and maintained an average effluent concentration around half the magnitude of the influent concentration throughout the growth phase (fluctuations are bound by $\sim 1.5 - 6\ mg/L$).
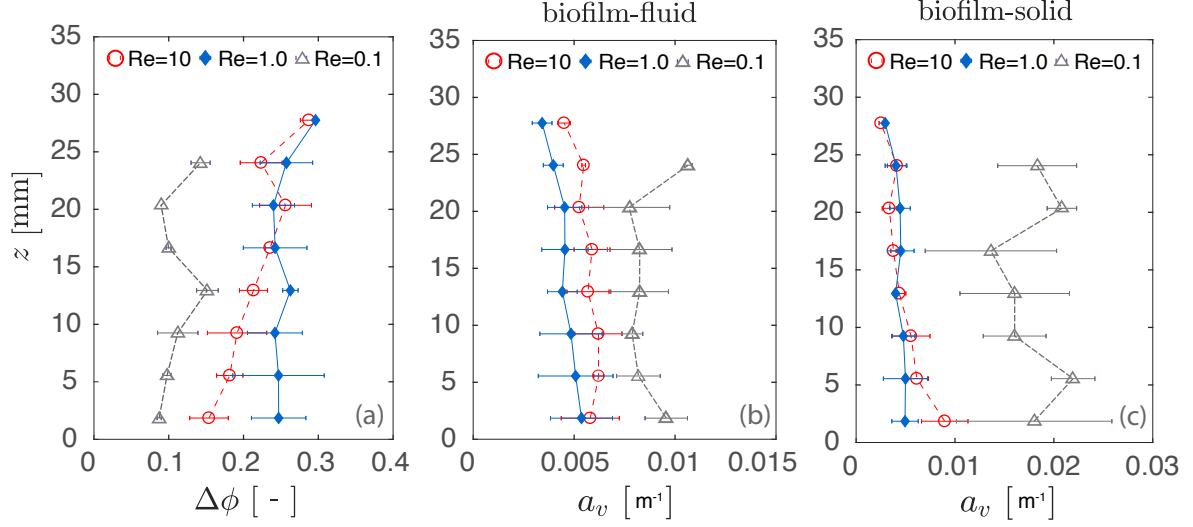
Figure 4: Spatial distribution of porosity change (a), biofilm-fluid surface area per volume (b), and biofilm-solid surface area per volume (c). Data points represent the averages of two experiments at individual sections. Error bars represent one standard deviation.

3.3. Structural evolution of the pore space

In order to characterize the nature of biofilm growth at different flow rates, the axial distributions of a number of structural measures were studied. Spatial profiles for these measures along the flow direction are plotted in Figure 4. The change in porosity in a column (before and after growth) is the most obvious metric to indicate the amount of bioclogging. Figure 4a shows that the intermediate flowrate ($Re = 1.0$) resulted in the largest reduction in porosity, followed by the highest ($Re = 10$), and lowest flowrates ($Re = 0.1$), respectively. The profiles in Figure 4 further show that the extent of porosity reduction varied along the axial direction (z) in all six test cases, but less extensively so at the lowest flow rate. The three-dimensional visualizations shown in Figure 4 are in clear agreement with these findings as a significantly lesser amount of biofilm is observed in the $Re = 0.1$ columns, and a denser and greater volume of biofilm is observed in the $Re = 1.0$ columns. It is also worth noting that we are able to distinguish the direction of flow (upwards) from the images, and observe
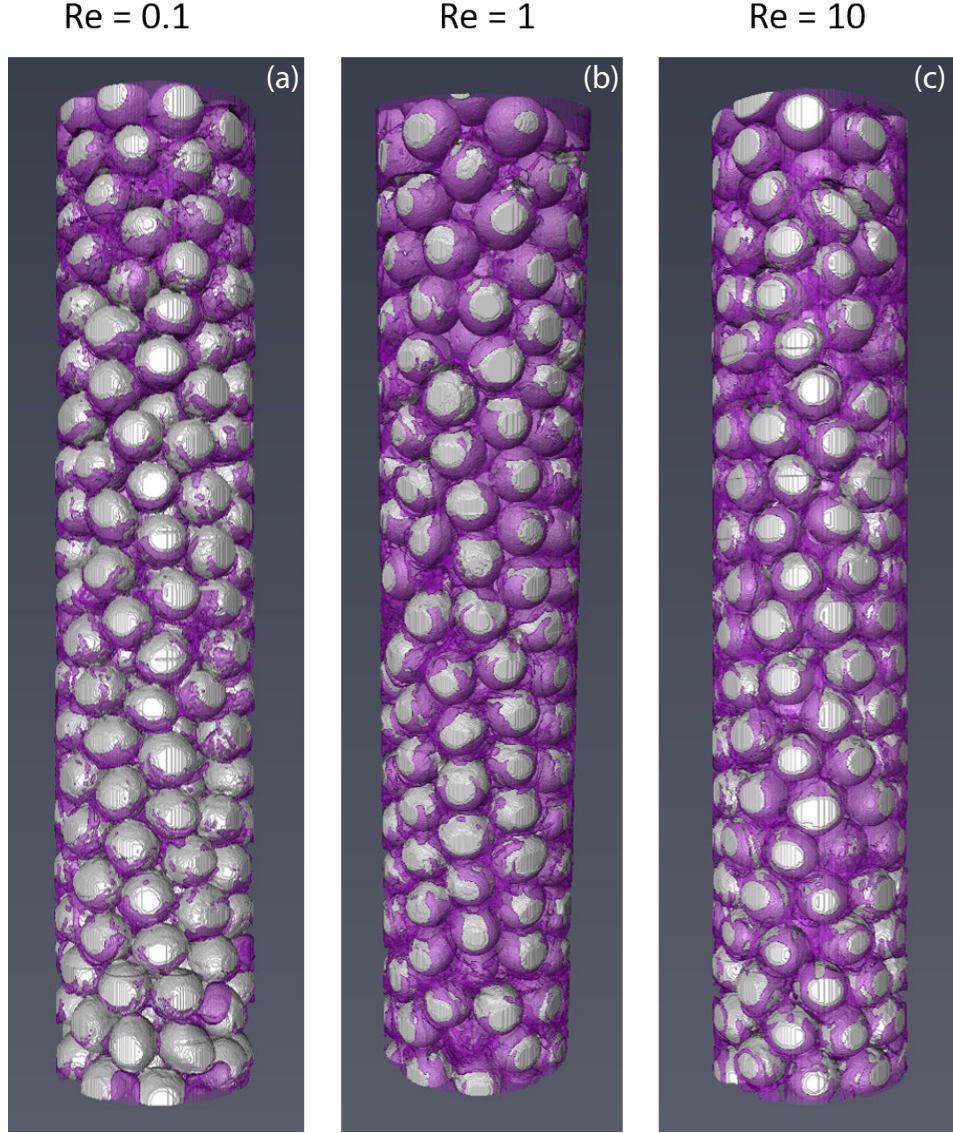
21

Re = 0.1   Re = 1   Re = 10

Figure 5: Visualizations of biofilm distribution in columns subject to $Re = 0.1$ (a), $Re = 1.0$ (b), and $Re = 10$ (c). Glass beads are gray, and biofilm is purple in the online version.

less rigorously attached features such as streamers (Drescher et al., 2013), despite the concern mentioned in the introduction that the $BaSO_4$ method may scour or detach such more weakly attached biofilm components when the contrast agent is added to the columns. We further examined the biofilm-solid, and biofilm-fluid interfacial areas per unit volume. Figures 4b-c show that these measures are fairly similar for the $Re = 1.0$ and $Re = 10$ columns, but slightly larger for $Re = 0.1$ columns.

In order to assess biofilm formation in planes transverse to the flow direction, we calculated the percentage of the total attachment surface area which is associated with the biofilm that is fixed on the sidewalls of each column section as opposed to being attached to the surface of glass beads within the same section. This measure provides some indication of the lateral distribution of biofilm and the degree of penetration of biofilm into the glass bead matrix. The results indicate that a significantly larger fraction of biofilm was attached to the column sidewalls at the highest flow rate ($>$ 35% in the first 10 mm of the test section) compared with the intermediate flow rate columns ($\sim$27% in the first 10 mm of column elevation) (Figure 6a). This difference was observed for total average biofilm volumes of 0.061 cm^3 and 0.085 cm^3 for the highest and intermediate flow rates respectively in the first 10 mm of the columns. Percent sidewall attachment for the lowest flow rate was relatively invariant in the axial direction. In contrast, the values for the intermediate and highest flow rates show a consistent decrease ($\sim$ 10%) toward the outlet.

The three structure indices highlight different aspects of changing biofilm configurations with changing flow rates. There was a consistent trend towards higher connectivity indices (CI) with increasing Re (Figure 6b). At $Re = 0.1$ biofilm connectivity was lowest ($CI \leq 1$) because the volume fraction of biofilm was also lowest, biomass being distributed in smaller, isolated patches. At intermediate flow rates ($Re = 1$) the biofilm had a much higher connectivity ($1 < CI < 3$), because the biofilm occupied the pore space almost completely (lowest porosity in Figure 4b). There was a gradual reduction in connectivity with inlet distance, because the biofilm gets more compact. That is, since flow paths occupied by $BaSO_4$ solution decreased with inlet distance, there were less redundant loops in the biofilm around these flow paths. This CI reduction with inlet distance is in line with decreasing porosity and decreasing reactive surface area (Figure 4b-c). The $Re = 10$ columns exhibited the opposite trend of increasing connectivity starting at small isolated patches directly at the inlet ($CI \approx 1$) and ending with the highest connectivity of all columns in the upper part ($CI > 3$) because biofilm and flow channels of $BaSO_4$ for complex intermingled structures also exhibited the highest

reactive surface area (Figure 4c).

The differences in the solid distance indices were less pronounced (Figure 6c). In general, $SDI \leq 1$ because biofilm growth was always initiated on solid surfaces so that biofilm had a tendency to be located close to solid interfaces. The SDI was highest at intermediate flow rates because the biofilm occupied the largest part of the pore space so that the average distance of the biofilm e_{bf} approached that of the pore space e_{ps}. Both the highest ($Re = 10$) and lowest ($Re = 0.1$) flow rate exhibited a gradual increase in SDI from the inlet towards the outlet. In both cases biofilm clusters directly at the inlet were small and directly attached to grain surfaces. With increasing inlet distance the volume fraction and surface area also increased and so did the growth into pore centers (Figure 4b-c). Directly at the outlet there was a consistent increase in SDI among all columns that might be caused by accumulation of biomass. The pore size index (PSI) exhibited very similar behavior and therefore carried redundant information at least for the investigated glass bead medium (Figure 6d). There was a tendency of the biofilm to occupy smaller pore constrictions for all flow rates, which was less pronounced at intermediate flow rates ($Re = 1$) because at these high volume fractions the average pore diameter covered by the biofilm (d_{bf}) approached that of the entire pore space (d_{ps}). At the highest flow rate ($Re = 10$) there was again a gradual increase in PSI with inlet distance, because in the upper part of the column biofilm growth or accumulation extended more towards bigger pore bodies.

3.4. Bioclogging

Figure 7 shows the comparison between transducer-based and image-based hydraulic conductivities before and after bacterial growth. The shaded areas in the figure represent the uncertainty bounds of the transducer-based measurements due to potential growth in the inlet tubing, computed as described in Section 2.8. The transducer-measured change in hydraulic conductivity varied between 1 to 2 orders of magnitude for all columns, values that are comparable to the range reported in other investigations (e.g. Cunningham et al. (1991); Seifert and Engesgaard (2007); Thullner (2010)). The largest mean decrease in K was observed for the $Re = 1.0$ columns while the lowest flow
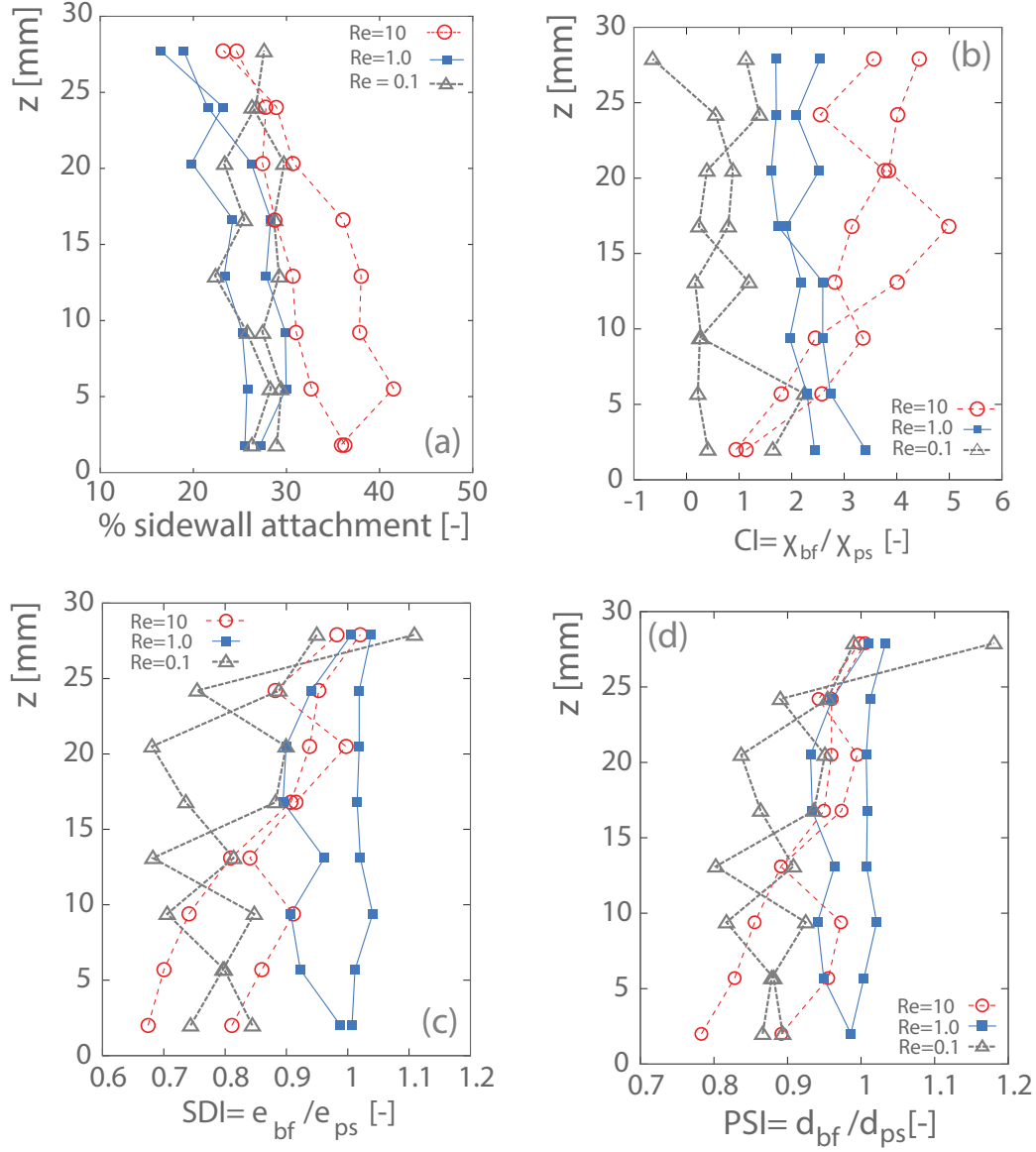
Figure 6: Spatial distributions of the contribution of sidewall attachment to the total biofilm attachment surface area (a), the normalized connectivity index (b), the solid distance index (c), and the pore size index (d).

rate columns ($Re = 0.1$) produced the smallest mean decrease in hydraulic conductivity. Figure 7a shows that the Kozeny-Carman relationship with $1/\beta\tau^2 = 1/5$ (model A) predicted the *trend* of reduction in K at the different flow rate, but tended to systematically underestimate the magnitudes compared with transducer-based measurements, despite the prefactor being representative at the onset of the experiments.

25

A potential cause of the observed deviation between the two methods is an increase in the tortuosity of the media after bacterial growth. We calculated the pre- and post-growth tortuosities directly from the images using the Centroid Path Tortuosity module in Avizo Fire 8.3. This module computes the tortuosity of a path formed by the centroids on each plane along the z-axis of a binary 3D image. The biofilm and solid phases were combined in the image and then the image was binarized before the tortuosity was calculated for each stack of images. An average of the two columns for each flow rate is presented in Figure 7b (values are normalized by pre-growth tortuosities computed using the same method). The computed values were then used to correct the prefactor in the Kozeny-Carman relationship (model B). Figure 7c shows that accounting for an increase in tortuosity significantly improved the comparison between transducer-based and image-based computations of post-growth hydraulic conductivity for all flow rates. The observed increase in tortuosity is slightly larger than the range of values obtained via simulations of 2D random media for $\varphi < 0.3$ (Hyman et al., 2012; Matyka et al., 2008).

4. Discussion

A combination of results from different measurements supports the hypothesis that growth under $Re = 0.1$ was significantly nutrient-limited. The almost complete depletion of dissolved oxygen at this flowrate (Figure 3) supports this picture, although biofilm growing in the inlet tubing could have contributed to the consumption of inlet DO, and thereby have contributed to the recorded pressure drops. Limited growth at $Re = 0.1$ is also reflected in the markedly lower reduction in porosity (Figure 4d, and Figure 5a) and hydraulic conductivity when compared with higher flow rates. The average biofilm volume at this flow rate is relatively uniform axially with low connectivity among dispersely distributed biofilm clusters that are preferentially attached to grain boundaries and pore constrictions. Sensitivity of biofilm structure to the availability of oxygen has been reported previously (e.g. Chang et al. (2015)).

In contrast, biofilm growth is improved at the intermediate and highest flow rates
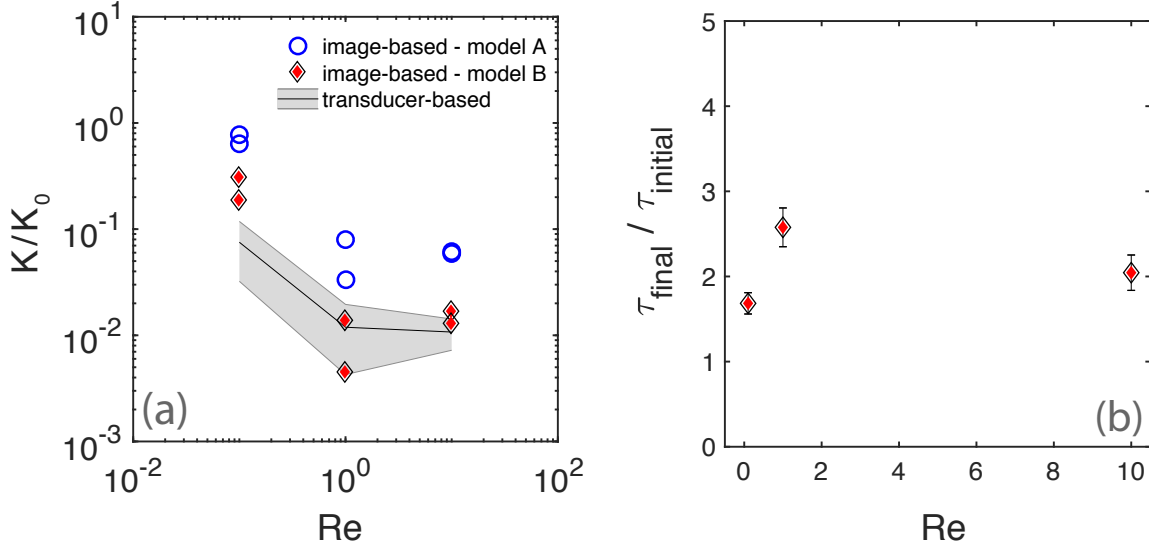
Figure 7: (a): Transducer-based and image-based estimates for reduction in hydraulic conductivity at different flow rates. Image-based results are calculated using Eq 11 with $1/\beta\tau^2 = 1/5$ (model A), and tortuosity values directly computed from images (model B). The shaded area shows the potential uncertainty in transducer-based measurements due to growth in inlet tubings. (b): Ratios of pre- and post-growth tortuosities obtained via direct analysis of images.

(compare Figure 5a, b and c). We observed a gradient in average biofilm volume that increased toward the top of the columns at $Re = 1.0$ and 10, a likely indication of shear-induced sloughing of cells and subsequent accumulation near the outlet (an 1/8-inch narrow opening that connects the porous section to external tubing). Interestingly other gradients in biofilm configurations showed opposite trends for $Re = 0.1$ and $Re = 10$. At intermediate flow rates the biofilm growth was more evenly distributed within the pore space in terms of occupied pore sizes and grain distances. The reactive surface area and connectivity decreased slightly towards the outlet. At the highest flow rate, in turn, there was a distinct shift towards growth in pore constrictions and along grain surfaces especially close to the inlet as well as a distinct increase in biofilm volume, reactive surface and connectivity with inlet distance. A more subtle form of heterogeneity is evident in the average percent sidewall attachment, which decreased significantly beyond the first few sections for $Re = 1.0$ and 10, and is invariant for $Re = 0.1$. These trends suggest that, especially under the higher shear flows, biofilm

27

growth undergoes a transition where regions near the sidewall are increasingly less occupied by biofilm toward the outlet. This is because pores along the sidewalls are wider than pores between glass beads due to sub-optimal packing and they therefore impose a lower resistance to flow.

The inhomogeneities in the spatial distribution of biofilms appear to be linked to regions where dramatic changes in flow take place. The three examples observed here are (i) the increased tendency of biofilms to form in the sidewall regions near the inlet. This tendency could be a consequence of the generally higher concentrations of dissolved oxygen near the inlet, and the flow field still being affected by the converging-diverging nozzle-like structure of the column inlet; (ii) accumulation of biofilm near the outlet where flow is converging into a more constricted opening as discussed above; and (iii) at the highest flow rate the tendency of biofilm to occupy pore constrictions and grain surfaces directly close the inlet, an effect that disappears again at greater inlet distances. This indicates that higher shear flows in the main flow paths near the inlet hinders the biofilm from occupying the center of bigger pore bodies in the vicinity of the inlet.

The fact that correcting for tortuosity significantly improves the comparison between transducer- and image-based post-growth permeabilities supports the notion that biofilm growth can completely transform the structure of pore-scale flow (Drescher et al., 2013). The image-based measurements for $Re = 0.1$ and $Re = 10$ can potentially be further improved by using other pore space attributes than the harmonic mean of porosities. One way forward would be to compute critical path conductivities (Friedman and Seaton, 1996), by searching for the lowest conductivity along the path of lowest flow resistance, which in our study would likely be situated close to the outlet were biofilm was accumulating. Although the volume fraction and associated porosity of this type of local growth is small, it can impose a dominant impact on effective permeability. Similar results have been reported by Bielefeldt et al. (2002) where decreases in hydraulic conductivity of up to 3 orders of magnitude were observed despite a mere $3 - 8$ percent decrease in porosity due to biofilm growth.

We should note that the transducer-derived post-growth permeabilities carry some

uncertainty as well, because observed fluctuations make it difficult to obtain an accurate value for pressure drop immediately before the termination of the experiment. Implementing an averaging window adjacent to the end of the experiment can stabilize the reading, but introduces information from earlier times that might not necessarily represent the snapshot studied after imaging. Considering this and the simplicity of the Kozeny-Carman model, image-based calculations demonstrate very good accuracy. Once actual tortuosities were used to predict the reduction in hydraulic conductivity, the trend with Re was very well-matched (model B in Figure 7).

Based on the overall pattern of reduction in hydraulic conductivity at different flow rates, we hypothesize that the bioclogging was influenced by a trade-off between the availability of nutrients (mainly dissolved oxygen) and shear-induced sloughing. Biofilms grown under an initial Re of 1.0 resulted in a slightly larger average reduction in hydraulic conductivity and porosity. Both parameters decreased as flow rate increased in the current round of experiments. Our interpretation of this trend is that, as flow rate increased, a threshold was crossed at which point oxygen is no longer a limiting factor in biofilm growth, and continuous growth was promoted until shear stress induced by the increasingly restricted flow initiates sloughing.

5. Limitations and Future Work

Balancing complete coverage of the pore space by the contrast agent, while minimizing sloughing of biomass is the primary challenge during imaging. The image processing workflow implemented here enabled a significant improvement in the accuracy of phase segmentation over previous efforts by accounting for the heterogeneities in the spatial distribution of the barium sulfate contrast agent. Development of more sophisticated contrast agents and tailored image processing algorithms could further improve the resolution of the method and reduce its intrusivity. Because we use microimaging as a model-driven predictor, the sensitivity of image-based measurements depends on the complexity of the models used to deduce them. We would expect that using models that carry more information on the morphology of the pore space significantly im-

prove the accuracy of the method, perhaps beyond what is possible using transducer measurements. For instance one could directly take into account local variations in velocity and pressure and their effect on permeability in a direct numerical simulation of the post-growth flow field (e.g. Peszynska et al. (2015)). Regardless, computations of permeability/hydraulic conductivity using the Kozeny-Carman model and the measured surface-area-to-volume ratios, porosity, and tortuosity (all purely image-based measurements) demonstrated very promising fidelity.

Another step toward better understanding the morphology, distribution and quantity of biomass growing within porous structures is to systematically study a broader range of flow rate and nutrient conditions, with each condition replicated several times. In this perspective, the present results show great promise for future use of the method in understanding the reported heterogeneities in physical properties of porous media subject to microbial growth (e.g. acoustic signatures, complex conductivity, etc.) and the post-growth 3D structure of the pore space (Abdel Aal et al., 2010; Atekwana and Slater, 2009; Davis et al., 2006, 2009, 2010). Imaging of relatively large samples were achieved here, enabling the study of bulk growth indicators in response to a prescribed flow rate, as well as local variations in growth in the model systems. New structural indices were introduced that cover very different aspects of biofilm configurations, facilitating systematic studies in the future. The degree to which these results are generalizable inevitably depends on the choices made during the design of the experimental system, so future work can focus on more complex pore structures and exploring a broader range of replicated conditions.

6. Conclusions

3D visualization of biofilm structure was achieved for three distinct hydrodynamic conditions in opaque porous media. Microimaging was used to track the structural changes of the pore spaces due to biofilm growth, which were cross-referenced with bulk measurements of pressure drop and oxygen utilization. Distinct growth and local morphological patterns were observed for growth in columns subject to different flow

rates. Excellent agreement was found between transducer-derived hydraulic conductivities and image-based estimates using a simple porosity-permeability relationship prior to growth. Post-growth permeabilities proved more challenging to predict due possibly to the development of heterogeneities in pore morphology. Yet, very good agreement was observed between the trends of hydraulic conductivity reduction at different flow rates using the two methods, and the results improved when the increased (actual) post-growth tortuosity of the pore space was accounted for. Bioclogging was found to depend non-trivially on flow rate, likely a function of competing mass transfer (dissolved oxygen delivery) and shear stress. The use of a barium sulfate suspension as a contrast agent was further fine-tuned by implementing a novel image processing workflow that accounts for inhomogeneities in the attenuation of the fluid phase. The results demonstrate the utility of microimaging using X-ray CT in studies of transformation of porous media subject to biofilm growth.

Acknowledgements

Nomenclature

φ	porosity
ρ	fluid density
$v_s \equiv v_z$	(stream-wise) superficial (Darcy) velocity
D	pore radius ($\equiv$ characteristic length scale)
μ	fluid viscosity
Re	Reynolds number
Q	volumetric flow rate
A	cross-sectional area
κ_{zz}	stream-wise component of the permeability tensor
p	hydrodynamic pressure
g	acceleration due to gravity
K	column hydraulic conductivity
Φ	Hubbert's potential (hydraulic head)
L	column length
ΔP	net pressure difference across column
τ	tortuosity
$\mathcal{S}$	interfacial area to volume ratio
β	constant in the Kozeny-Carman model
Ω	set of all voxels
Π	set of all pairs of neighboring voxels
Λ	set of image sources
$c(\mathbf{x})$	class label of voxel at point $\mathbf{x}$
$\mu_{c,\lambda}$	class mean in image λ
σ^2	class variance in image λ
$I'_\lambda(\mathbf{x})$	gray value of voxel $\mathbf{x}$ in image λ
χ	Euler characteristic
$\mathcal{N}$	number of isolated objects in a material of interest
$\mathcal{L}$	number of redundant connections within all material clusters
$\mathcal{O}$	number of cavities in a material of interest
d_α	average pore diameter in phase α
e_α	average distance within phase α
CI	the connectivity index
PSI	the pore size index
SDI	the solid distance index

References

G. Z. Abdel Aal, E. A. Atekwana, and E. A. Atekwana. Effect of bioclogging in porous media on complex conductivity signatures. *Journal of Geophysical Research: Biogeosciences*, 115(G3), 2010.

R. T. Armstrong and D. Wildenschild. Investigating the pore-scale mechanisms of microbial enhanced oil recovery. *Journal of Petroleum Science and Engineering*, 94: 155–164, 2012.

E. A. Atekwana and L. D. Slater. Biogeophysics: A new frontier in earth science research. *Reviews of Geophysics*, 47(4), 2009.

P. Baveye. Comment on 'comparison of bioclogging effects in saturated porous media within one-and two-dimensional flow systems' by martin thullner. *Ecological Engineering*, 36(6):835–836, 2010.

P. Baveye, P. Vandevivere, B. L. Hoyle, P. C. DeLeo, and D. S. de Lozada. Environmental impact and mechanisms of the biological clogging of saturated soils and aquifer materials. *Critical Reviews in Environmental Science and Technology*, 28(2): 123–191, 1998.

P. C. Baveye and C. Darnault. Microbial competition and evolution in natural porous environments: Not that simple. *Proceedings of the National Academy of Sciences*, page 201700992, 2017.

J. Bear. *Dynamics of fluids in porous media*. Courier Corporation, 2013.

H. Beyenal, C. Donovan, Z. Lewandowski, and G. Harkin. Three-dimensional biofilm structure quantification. *Journal of Microbiological Methods*, 59(3):395–413, 2004.

A. R. Bielefeldt, C. McEachern, and T. Illangasekare. Hydrodynamic changes in sand due to biogrowth on naphthalene and decane. *Journal of Environmental Engineering*, 128(1):51–59, 2002.

M. Carrel, M. A. Beltran, V. L. Morales, N. Derlon, E. Morgenroth, R. Kaufmann, and M. Holzner. Biofilm imaging in porous media by laboratory x-ray tomography: Combining a non-destructive contrast agent with propagation-based phase-contrast imaging tools. *PloS one*, 12(7):e0180374, 2017.

Y.-W. Chang, A. A. Fragkopoulos, S. M. Marquez, H. D. Kim, T. E. Angelini, and A. Fernández-Nieves. Biofilm formation in geometries with different surface curvature and oxygen availability. *New Journal of Physics*, 17(3):033017, 2015.

K. Z. Coyte, H. Tabuteau, E. A. Gaffney, K. R. Foster, and W. M. Durham. Reply to baveye and darnault: Useful models are simple and extendable. *Proceedings of the National Academy of Sciences*, page 201702303, 2017.

A. B. Cunningham, W. G. Characklis, F. Abedeen, and D. Crawford. Influence of biofilm accumulation on porous media hydrodynamics. *Environmental Science & Technology*, 25(7):1305–1311, 1991.

C. A. Davis, E. Atekwana, E. Atekwana, L. D. Slater, S. Rossbach, and M. R. Mormile. Microbial growth and biofilm formation in geologic media is detected with complex conductivity measurements. *Geophysical Research Letters*, 33(18), 2006.

C. A. Davis, L. J. Pyrak-Nolte, E. A. Atekwana, D. D. Werkema, and M. E. Haugen. Microbial-induced heterogeneity in the acoustic properties of porous media. *Geophysical Research Letters*, 36(21), 2009.

C. A. Davis, L. J. Pyrak-Nolte, E. A. Atekwana, D. D. Werkema, and M. E. Haugen. Acoustic and electrical property changes due to microbial growth and biofilm formation in porous media. *Journal of Geophysical Research: Biogeosciences*, 115(G3), 2010.

Y. Davit, G. Iltis, G. Debenest, S. Veran-Tissoires, D. Wildenschild, M. Gérino, and M. Quintard. Imaging biofilm in porous media using x-ray computed microtomography. *Journal of Microscopy*, 242(1):15–25, 2011.

Y. Davit, H. Byrne, J. Osborne, J. Pitt-Francis, D. Gavaghan, and M. Quintard. Hydrodynamic dispersion within porous biofilms. *Physical Review E*, 87(1):012718, 2013.

K. Drescher, Y. Shen, B. L. Bassler, and H. A. Stone. Biofilm streamers cause catastrophic disruption of flow with consequences for environmental and medical systems. *Proceedings of the National Academy of Sciences*, 110(11):4345–4350, 2013.

C. Dreszer, A. D. Wexler, S. Drusová, T. Overdijk, A. Zwijnenburg, H.-C. Flemming, J. C. Kruithof, and J. S. Vrouwenvelder. In-situ biofilm characterization in membrane systems using optical coherence tomography: Formation, structure, detachment and impact of flux change. *Water Research*, 67:243–254, 2014.

S. R. du Roscoat, J. Martins, P. Séchet, E. Vince, P. Latil, and C. Geindreau. Application of synchrotron x-ray microtomography for visualizing bacterial biofilms 3d microstructure in porous media. *Biotechnology and Bioengineering*, 111(6):1265–1271, 2014.

S. P. Friedman and N. A. Seaton. On the transport properties of anisotropic networks of capillaries. *Water Resources Research*, 32(2):339–347, 1996.

P. R. Gunjal, V. V. Ranade, and R. V. Chaudhari. Computational study of a single-phase flow in packed beds of spheres. *AIChE Journal*, 51(2):365–378, 2005.

A. L. Herring, L. Andersson, S. Schlüter, A. Sheppard, and D. Wildenschild. Efficiently engineering pore-scale processes: The role of force dominance and topology during nonwetting phase trapping in porous media. *Advances in Water Resources*, 79:91–102, 2015.

J. D. Hyman, P. K. Smolarkiewicz, and C. L. Winter. Heterogeneities of flow in stochastically generated porous media. *Physical Review E*, 86(5):056701, 2012.

G. C. Iltis. *Visualization and characterization of biofilm spatial distribution in porous media using x-ray computed microtomography*. PhD thesis, 2013.

G. C. Iltis, R. T. Armstrong, D. P. Jansik, B. D. Wood, and D. Wildenschild. Imaging biofilm architecture within porous media using synchrotron-based x-ray computed microtomography. *Water Resources Research*, 47(2), 2011.

T. Ivankovic, S. R. du Roscoat, C. Geindreau, P. Séchet, Z. Huang, P. Charier, and J. M. Martins. Laboratory x-ray microtomography as a tool for 3d visualization of biofilm in porous media made up of zeolite. In *Microbiology Society Annual Conference 2017*, 2017.

D.-S. Kim and H. S. Fogler. Biomass evolution in porous media and its effects on permeability under starvation conditions. *Biotechnology and Bioengineering*, 69(1): 47–56, 2000.

R. Kulkarni, M. Tuller, W. Fink, and D. Wildenschild. Three-dimensional multiphase segmentation of x-ray ct data of porous materials using a bayesian markov random field framework. *Vadose Zone Journal*, 11(1):0–0, 2012.

A. P. Leis, S. Schlicher, H. Franke, and M. Strathmann. Optically transparent porous medium for nondestructive studies of microbial biofilm architecture and transport dynamics. *Applied and Environmental Microbiology*, 71(8):4801–4808, 2005.

Z. Li, A. A. Hassan, E. Sahle-Demessie, and G. A. Sorial. Transport of nanoparticles with dispersant through biofilm coated drinking water sand filters. *Water research*, 47(17):6457–6466, 2013.

P. D. Majors, J. S. McLean, J. K. Fredrickson, and R. A. Wind. Nmr methods for in-situ biofilm metabolism studies: spatial and temporal resolved measurements. *Water Science & Technology*, 52(7):7–12, 2005.

B. Manz, F. Volke, D. Goll, and H. Horn. Measuring local flow velocities and biofilm structure in biofilm systems with magnetic resonance imaging (mri). *Biotechnology and bioengineering*, 84(4):424–432, 2003.

M. Matyka, A. Khalili, and Z. Koza. Tortuosity-porosity relation in porous media flow. *Physical Review E*, 78(2):026306, 2008.

T. R. Neu and J. R. Lawrence. Innovative techniques, sensors, and approaches for imaging biofilms at different scales. *Trends in Microbiology*, 23(4):233–242, 2015.

M. Peszynska, A. Trykozko, G. Iltis, S. Schlueter, and D. Wildenschild. Biofilm growth in porous media: experiments, computational modeling at the porescale, and upscaling. *Advances in Water Resources*, 2015.

B. E. Rittmann. The significance of biofilms in porous media. *Water Resources Research*, 29(7):2195–2202, 1993.

S. J. Rodríguez and P. L. Bishop. Three-dimensional quantification of soil biofilms using image analysis. *Environmental Engineering Science*, 24(1):96–103, 2007.

P. Rosin. Unimodal thresholding. *Pattern Recognition*, 34(11):2083–2096, 2001.

S. Schlüter, A. Sheppard, K. Brown, and D. Wildenschild. Image processing of multiphase images obtained via x-ray microtomography: a review. *Water Resources Research*, 50(4):3615–3639, 2014.

D. Seifert and P. Engesgaard. Use of tracer tests to investigate changes in flow and transport properties due to bioclogging of porous media. *Journal of Contaminant Hydrology*, 93(1):58–71, 2007.

R. Sen. Biotechnology in petroleum recovery: the microbial eor. *Progress in energy and combustion Science*, 34(6):714–724, 2008.

J. D. Seymour, J. P. Gage, S. L. Codd, and R. Gerlach. Anomalous fluid transport in porous media induced by biofilm growth. *Physical review letters*, 93(19):198103, 2004.

J. D. Seymour, J. P. Gage, S. L. Codd, and R. Gerlach. Magnetic resonance microscopy of biofouling induced scale dependent transport in porous media. *Advances in water resources*, 30(6):1408–1420, 2007.

T. L. Stewart and H. S. Fogler. Biomass plug development and propagation in porous media. 2001.

P. Stoodley, Z. Lewandowski, J. D. Boyle, and H. M. Lappin-Scott. Structural deformation of bacterial biofilms caused by short-term fluctuations in fluid shear: an in situ investigation of biofilm rheology. *Biotechnology and Bioengineering*, 65(1):83–92, 1999.

K. M. Thormann, R. M. Saville, S. Shukla, D. A. Pelletier, and A. M. Spormann. Initial phases of biofilm formation in shewanella oneidensis mr-1. *Journal of bacteriology*, 186(23):8096–8104, 2004.

K. M. Thormann, R. M. Saville, S. Shukla, and A. M. Spormann. Induction of rapid detachment in shewanella oneidensis mr-1 biofilms. *Journal of bacteriology*, 187(3): 1014–1021, 2005.

M. Thullner. Comparison of bioclogging effects in saturated porous media within one- and two-dimensional flow systems. *Ecological Engineering*, 36(2):176–196, 2010.

D.-M. Tsai. A fast thresholding selection procedure for multimodal and unimodal histograms. *Pattern Recognition Letters*, 16(6):653 – 666, 1995. ISSN 0167-8655. doi: 10.1016/0167-8655(95)80011-H.

P. Vandevivere and P. Baveye. Saturated hydraulic conductivity reduction caused by aerobic bacteria in sand columns. *Soil Science Society of America Journal*, 56(1): 1–13, 1992.

P. Vandevivere, P. Baveye, D. S. Lozada, and P. DeLeo. Microbial clogging of saturated soils and aquifer materials: Evaluation of mathematical models. *Water Resources Research*, 31(9):2173–2180, 1995.

K. Venkateswaran, D. P. Moser, M. E. Dollhopf, D. P. Lies, D. A. Saffarini, B. J. MacGregor, D. B. Ringelberg, D. C. White, M. Nishijima, H. Sano, J. Burghardt, E. Stackerbrandt, and K. H. Nealson. Polyphasic taxonomy of the genus shewanella and description of *shewanella oneidensis* sp. nov. *International Journal of Systematic and Evolutionary Microbiology*, 49(2):705–724, 1999.

H.-J. Vogel, U. Weller, and S. Schlüter. Quantification of soil structure based on minkowski functions. *Computers & Geosciences*, 36(10):1236–1245, 2010.

S. J. Vogt, A. B. Sanderlin, J. D. Seymour, and S. L. Codd. Permeability of a growing biofilm in a porous media fluid flow analyzed by magnetic resonance displacement-relaxation correlations. *Biotechnology and bioengineering*, 110(5):1366–1375, 2013.

D. von der Schulenburg, T. Pintelon, C. Picioreanu, M. Van Loosdrecht, and M. Johns. Three-dimensional simulations of biofilm growth in porous media. *AIChE Journal*, 55(2):494–504, 2009.

M. Wagner, D. Taherzadeh, C. Haisch, and H. Horn. Investigation of the mesoscale structure and volumetric features of biofilms using optical coherence tomography. *Biotechnology and Bioengineering*, 107(5):844–853, 2010.

D. Wildenschild and A. P. Sheppard. X-ray imaging and analysis techniques for quantifying pore-scale structure and processes in subsurface porous medium systems. *Advances in Water Resources*, 51:217–246, 2013.

C. Xi, D. Marks, S. Schlachter, W. Luo, and S. A. Boppart. High-resolution three-dimensional imaging of biofilm development using optical coherence tomography. *Journal of Biomedical Optics*, 11(3):034001–034001, 2006.

R. Yarwood, M. L. Rockhold, M. Niemet, J. S. Selker, and P. J. Bottomley. Noninvasive quantitative measurement of bacterial growth in porous media under unsaturated-flow conditions. *Applied and Environmental Microbiology*, 68(7):3597–3605, 2002.

J. C. Young and M. F. Dahab. Effect of media design on the performance of fixed-bed anaerobic reactors. *Water Science and Technology*, 15(8-9):369–383, 1983.

7. Appendix

7.1. Segmentation of biofilm data

The challenge in segmenting biofilm images is that the $BaSO_4$ particles are non-uniformly distributed in the pore space that is not occupied by the biofilm (Fig. 1(a)). This results in broad range of intensities for the $BaSO_4$ phase. As a consequence, it cannot be identified as a third mode in the corresponding histogram (Fig. 1(d)). In turn, the difference between above-edge and below-edge intensity (Fig. 1(b)) is low for biofilm and beads, since in both phases the electron adsorption does not change with a small change in beam energy. Yet the difference is high for the $BaSO_4$ phase and varies with barium concentration. This results in a single peak for beads and biofilm and a long tailing for $BaSO_4$ in the corresponding histogram (Fig. 1(e)). The joint frequency distribution of the below-edge and the difference intensities (Fig. 1(g)) is already sufficient to identify beads as an isolated cluster in the feature space, but there is a gradual transition from biofilm to $BaSO_4$ due to the variation in barium concentration. This variation, however, can be assessed by the local image gradient (Fig. 1(b)), which is low in the homogeneous beads and biofilm and has a broad range of intensities in the $BaSO_4$ filled pore space. This leads to a joint peak at zero in the gradient histogram for biofilm and beads (Fig. 1(e)) and a long tail for $BaSO_4$ and the transition voxels at phase boundaries. The joint frequency distribution of the below-edge and the gradient intensities (Fig. 1(h)) exhibits two clusters at low gradient intensities, one for beads and one for biofilm, which are connected by an arch of partial volume voxels at the boundaries between the two phases, and extensive scattering for $BaSO_4$.

The two joint probabilites (Fig. 1(g,h)) are now used to estimate the class statistics in eq. 3 with the following workflow:

1. Unimodal thresholding (Rosin, 2001; Schlüter et al., 2014) is applied to separate the peak (biofilm and beads) from the tail ($BaSO_4$ and phase boundaries) in the gradient histogram. Note that this threshold corresponds to the horizontal line in Fig. 1(h). A ROI of voxels that belong to the peak class is created.
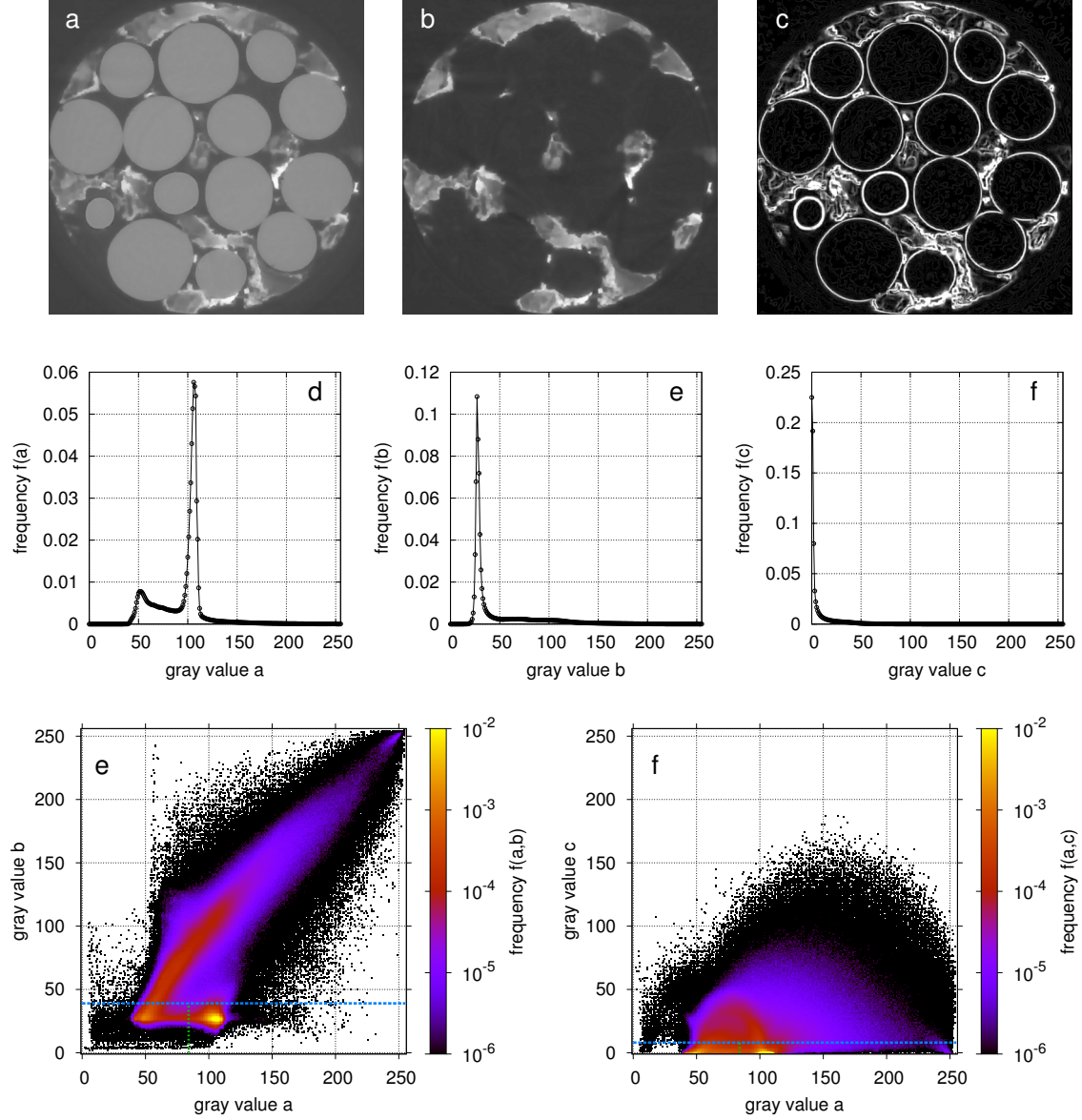
Figure 1: simple and joint frequency distributions for various input data: (a) 2D slice of a below-edge image from a medium flow rate (Re=1.0); (b) 2D slice of difference between above-edge and below-edge image; (c) 2D slice of gradient of below-edge image; (d) histogram of below-edge image; (e) histogram of difference image; (f) histogram of gradient image; (g) joint frequency distributions of below-edge and difference image including thresholds; (h) joint frequency distributions of below-edge and gradient image including thresholds

2. The histogram of below-edge intensities within this ROI is evaluated by a minimum search (Schlüter et al., 2014; Tsai, 1995) to detect the threshold between beads and biofilm. This corresponds to a vertical line in Fig. 1(h).

3. A bead label is assigned to all voxels that fulfill both threshold requirements and whose joint frequency exceeds a user-defined threshold, e.g. 1×10^{-3} in Fig. 1(h). Biofilm voxels are labelled in the same way.

4. Noise objects in the label image are removed with a size exclusion filter and the remaining labels are dilated with a spherical structure element of radius $r = 4$. The dilated areas are considered as phase boundaries and the rest is assigned to $BaSO_4$.

5. Steps 1-4 are repeated with the difference image instead of the gradient image as vertical axis in the feature space (Fig. 1(g)).

6. The final label image (Fig. 2(d)) is obtained by merging the label images from steps 4 and 5 together, i.e. labels that coincide in both images are kept and voxels with different labels are set back to unassigned.

7. The class statistics ($\mu_{c,\lambda}$ and $\sigma_{c,\lambda}^2$) in eq. 3 can then be estimated from label-specific histograms in each input image.

Note that the automated threshold detection methods in the presented workflow may fail, when the volume fraction of biofilm or $BaSO_4$ becomes too low. In that case that values have to be adapted manually. We are currently improving the workflow by substituting the iterative threshold detection for single source images with multi-dimensional clustering techniques that allow for irregular threshold surfaces in the feature space.

During Markov random field (MRF) segmentation each voxel is assigned a class label according to the penalty term for phase boundaries and the sum of likelihood terms of each class in eq. 3 (Fig. 2(a-c)). Due to reformulation the smallest value for the likelihood term is considered optimal. The likilihood term is multiplied with the user-defined weighting factor for each image source, which is set to a low value

of $\alpha_\lambda = 0.1, \lambda = 1, 2, 3$, to increase the penalty on phase boundaries and thus invoke smooth boundaries. The MRF segmentation results (Fig. 2(e)) are not optimal yet due to partial volume effects. That is, voxels along the bead boundaries are partially filled with biofilm, which leads to a false assignment to $BaSO_4$. Postprocessing has to be applied to remove this unwanted effect. To do so, a cubic kernel with 7^3 voxels loops through the image, detects boundaries as neighborhoods with more than one label and sets the central value to unassigned. Subsequently the labels are iteratively dilated back into unassigned areas by a simple majority rule, i.e. the most representative label in a cubic 7^3 kernel is assigned to the central voxel until no unassigned voxel is left. The result after postprocessing is depicted in Fig. 2(f).
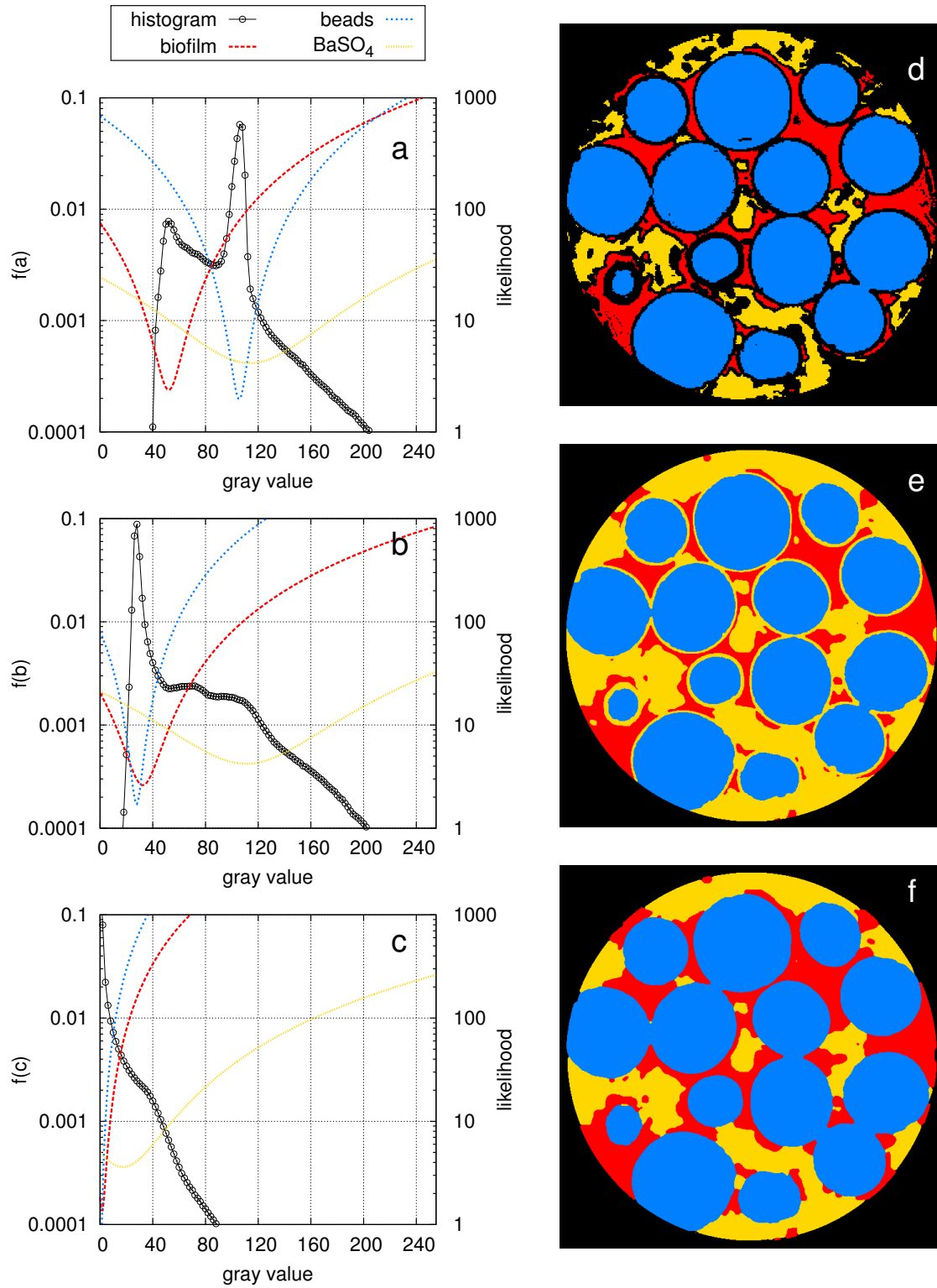
Figure 2: Segmentation and postprocessing results: likelihood of each class for a given gray value according to the class statistics in (a) the below-edge image, (b) the gradient image, (c) the difference image; (d) 2D slice of merged label image that serves as a template to estimate class statistics; (e) MRF segmentation results; (f) final egmentation results after postprocessing.

45